On the relationship between gas content, star formation, and global H I asymmetry of galaxies on the star-forming main-sequence

Adam B. Watts [1,2]★ Barbara Catinella [1,2] Luca Cortese [1,2] Chris Power [1,2] and Sara L. Ellison [3]

[1]*International Centre for Radio Astronomy Research, The University of Western Australia, Crawley, WA 6009, Australia*
[2]*ARC Centre of Excellence for All-Sky Astrophysics in 3 Dimensions (ASTRO3D), Australia*
[3]*Department of Physics & Astronomy, University of Victoria, Finnerty Road, Victoria, British Columbia V8P 1A1, Canada*

ABSTRACT

Observations have revealed that disturbances in the cold neutral atomic hydrogen (H I) in galaxies are ubiquitous, but the reasons for these disturbances remain unclear. While some studies suggest that asymmetries in integrated H I spectra (global H I asymmetry) are higher in H I-rich systems, others claim that they are preferentially found in H I-poor galaxies. In this work, we utilize the Arecibo Legacy Fast ALFA (ALFALFA) and extended GALEX Arecibo SDSS Survey (xGASS) surveys, plus a sample of post-merger galaxies, to clarify the link between global H I asymmetry and the gas properties of galaxies. Focusing on star-forming galaxies in ALFALFA, we find that elevated global H I asymmetry is not associated with a change in the H I content of a galaxy, and that only the galaxies with the highest global H I asymmetry show a small increase in specific star formation rate (sSFR). However, we show that the lack of a trend with H I content is because ALFALFA misses the 'gas-poor' tail of the star-forming main-sequence. Using xGASS to obtain a sample of star-forming galaxies that is representative in both sSFR and H I content, we find that global H I asymmetric galaxies are typically more gas-poor than symmetric ones at fixed stellar mass, with no change in sSFR. Our results highlight the complexity of the connection between galaxy properties and global H I asymmetry. This is further confirmed by the fact that even post-merger galaxies show both symmetric and asymmetric H I spectra, demonstrating that merger activity does not always lead to an asymmetric global H I spectrum.

Key words: galaxies: evolution – galaxies: ISM – galaxies: kinematics and dynamics – galaxies: star formation – radio lines: galaxies.

1 INTRODUCTION

The interstellar medium in star-forming galaxies is dominated by neutral atomic hydrogen (H I), which exists in a thin, rotationally supported disc. As H I is typically detectable to galactocentric radii a factor of 2–3 times higher than the bright optical component of galaxies (e.g. Wang et al. 2014), it is a sensitive tracer of external environmental mechanisms such as ram-pressure stripping or tidal interactions. The impact of these mechanisms is apparent in spatially resolved H I observations as asymmetric distributions of H I gas or deviations from ordered kinematics (e.g. Swaters et al. 1999; Chung et al. 2007), but the vast majority of H I observations are only spectrally (and not spatially) resolved. Global H I spectra carry little direct spatial information about the gas, but the signature of a disturbance none the less can be encoded in the shape of the emission line profile (e.g. Walter et al. 2008; de Blok et al. 2020; Reynolds et al. 2020a). Quantifying and interpreting these disturbances in global H I spectra, their relationship to galaxy properties, and whether they can be used to identify different evolutionary processes is vital to fully utilizing the next generation of blind H I surveys, which are predicted to detect over 500 000 global H I spectra (Koribalski et al. 2020).

Disturbances in the H I reservoirs in galaxies, measured through quantified asymmetry of global H I spectra (from here 'global H I asymmetry'), are commonplace (Richter & Sancisi 1994; Haynes et al. 1998; Espada et al. 2011), as ∼37 per cent of galaxies show significant global H I asymmetry after correcting for noise effects (Watts et al. 2020a). This has lead to numerous physical processes being proposed as their driving mechanisms, such as tidal interactions, gas accretion or removal, and lopsided dark matter haloes (see the review by Jog & Combes 2009, and references therein). In the isolated environment, a higher rate of global H I asymmetry has been found in late-type galaxies, which are typically more gas-rich (Haynes et al. 1998; Matthews, van Driel & Gallagher 1998; Espada et al. 2011). Galaxy pairs have been found to show higher global H I asymmetry compared to isolated galaxies (Bok et al. 2019), and Ellison, Catinella & Cortese (2018) found that post-merger galaxies are systematically H I-rich at fixed stellar mass. This has lead to the interpretation that H I asymmetry is higher in more gas-rich systems; and that gas accretion, which is stochastic in the local Universe (Sancisi et al. 2008), or accretion events such as mergers, could be the driving mechanisms.

However, recent work by Reynolds, Westmeier & Staveley-Smith (2020b) utilizing 1167 galaxies limited to the gas-rich regime from the H I Parkes All-Sky Survey (Barnes et al. 2001; Meyer et al. 2004; Wong et al. 2006) found no strong correlation between global H I asymmetry and H I content. An even more extreme result was

★ E-mail: 21146752@student.uwa.edu.au

found by Watts et al. (2020a), who analysed global H I asymmetry in the extended GALEX Arecibo SDSS Survey (xGASS; Catinella et al. 2018) and found that global H I asymmetries are actually more common in H I-poor galaxies. This apparent contradiction between the results of Watts et al. (2020a) and Reynolds et al. (2020b), and the higher asymmetry rates of late-type isolated galaxies and mergers likely originates from the different sample selections in these studies, and the galaxy environments to which they are sensitive. xGASS detects galaxies down to H I mass fractions ($M_{H I}/M_\star$) of $\sim$2 per cent in large group to small cluster environments, while isolated late-type galaxies and mergers are typically gas-rich systems. This demonstrates the need to quantify the relationship between galaxy properties and global H I asymmetry in systems that are not strongly affected by environment, namely gas-rich, star-forming galaxies.

In this work, we show how previous results are not in contradiction with each other once sample selection is taken into account. We take advantage of the Arecibo Legacy Fast ALFA (ALFALFA; Giovanelli et al. 2005; Haynes et al. 2018) blind H I survey, which by construction is biased towards detecting the most H I-rich objects in its volume, and thus samples the H I-rich regime with high statistics. We also include a sample of post-merger galaxies (Ellison et al. 2018) to explore the parameter space of systems undergoing strong gravitational interactions and the xGASS sample of Watts et al. (2020a) for context outside the gas-rich regime. By combining these three samples, our data are specifically designed to span a comprehensive range in H I fractions and level of disturbance. Utilizing this, we aim to determine how the H I and star formation content of galaxies change as a function of their global H I asymmetry.

This paper is formatted as follows. In Section 2 we describe our three data sets, and in Section 3 we describe our spectrum fitting, asymmetry measurements, quality cuts, population selections, and our method of comparing galaxy populations. Our results are presented in Section 4, and in Section 5 we discuss them in context with the literature, and conclude. All distance-dependant quantities in this work are computed assuming a flat Λ-Cold Dark Matter cosmology with $h = 0.7$, $\Omega_M = 0.3$, and $\Omega_\Lambda = 0.7$.

2 DATA SETS

2.1 ALFALFA sample

We identified the best optical counterparts in the Sloan Digital Sky Survey (SDSS; York et al. 2000) DR7 spectroscopic catalogue (Abazajian et al. 2009) to ALFALFA detected (code = 1) sources (Haynes et al. 2018) within 10 arcsec, and selected galaxies also covered by the *GALEX*-SDSS-Wide-field Infrared Survey Explorer (WISE) Legacy Master Catalogue (GSWLC-X2; Salim et al. 2016; Salim, Boquien & Lee 2018) within the following tolerances:

(i) $\log(M_\star/M_\odot) \geq 9$
(ii) $0.02 \leq z \leq 0.05$

The stellar mass selection is defined to cover the same range as xGASS (see 2.2); and the redshift selection is defined to avoid significant contributions from peculiar motions to recessional velocity measurements below $z = 0.02$, and the frequency range of the San Juan airport radar affecting ALFALFA observations above $z = 0.05$. In Section 3.1, we employ further selection cuts to make sure our results are not affected by artefacts in the data. We use stellar masses and star formation rates (SFRs) from the GSWLC-X2 catalogue as SFRs have been estimated using energy-balance constrained fitting of the UV/optical spectral energy distribution, plus infrared luminosity

of galaxies, as described in Salim et al. (2018). This is to avoid underestimation of the SFR derived from the centrally targeted SDSS fibre spectra in some massive star-forming galaxies (e.g. Cortese et al. 2020), which can host passive bulges at their centre while star formation proceeds as normal in the disc. The GSWLC-X2 catalogue is produced from the deepest UV data for each object in the *GALEX* shallow, medium, and deep catalogues, and is suited to studies of the star-forming main-sequence (SFMS) where UV emission is bright.

2.2 xGASS sample

xGASS (Catinella et al. 2018) is a stellar mass- and redshift-selected sample of 1179 galaxies in the ranges $10^9 \leq \log(M_\star/M_\odot) \leq 10^{10.5}$ and $0.01 \leq z \leq 0.05$. The parent sample is the overlap of the SDSS DR7 spectroscopic survey, the *GALEX* Medium Imaging Survey (Martin et al. 2005), and ALFALFA footprints. Galaxies not detected by ALFALFA were re-observed with targeted Arecibo observations until detected, or until an upper limit of $\sim$2$-$10 per cent in $M_{H I}/M_\star$ was reached (depending on galaxy stellar mass), making xGASS the deepest observations of cold gas in a representative sample of galaxies in the local Universe. Stellar masses in xGASS are from the Max Planck Institute for Astrophysics (MPA)/Johns Hopkins University (JHU) value-added catalogues (VAC) based on SDSS DR7, and SFRs are calculated from *GALEX* near-UV (NUV) plus WISE (Wright et al. 2010) mid-infrared fluxes as described in Janowiecki et al. (2017), and are comparable to the GSWLC-X2 catalogue used for ALFALFA. In this work, we use the sub-sample of xGASS detections presented in Watts et al. (2020a). Briefly, from the 804 xGASS detections (formal and marginal), seven galaxies were removed due to RFI overlapping the H I spectrum, and 108 H I confused galaxies were removed using the confusion flags in the xGASS catalogue as the detected H I is not meaningfully associated with the optical target. This left 689 galaxies in our xGASS sample, which we refine in Section 3.1.

2.3 Post-merger galaxies

We include a sample of merging galaxies identified as being in the post-coalescence phase (post-mergers) as presented and described in Ellison et al. (2018). Briefly, the sample consists of systems with $\log(M_\star/M_\odot) \geq 9$ and redshift $z < 0.04$ compiled from post-mergers identified in the Galaxy Zoo project by Darg et al. (2010) with extra quality control by Ellison et al. (2013), visual classification of SDSS galaxies by Nair & Abraham (2010), and visual inspection of galaxies with Simard et al. (2011) *r*-band asymmetry >0.05 by Ellison et al. (2018). Post-mergers without archival H I detections were re-observed with Arecibo using the same survey design as xGASS, resulting in a sample of 86 post-mergers with H I detections. We cross-matched these galaxies with GSWLC-X2 to get stellar masses and SFRs consistent with our ALFALFA sample, leaving 75 galaxies.

3 MEASUREMENTS AND POPULATION SELECTIONS

3.1 Spectrum fitting and asymmetry measurement

As in Watts et al. (2020a), we use the busy function (Westmeier et al. 2014) to parametrize our H I spectra. However, here we only use the fits to identify the edges of each spectrum, without attempting to optimize the fit to the shape of the H I profile. Examples of busy
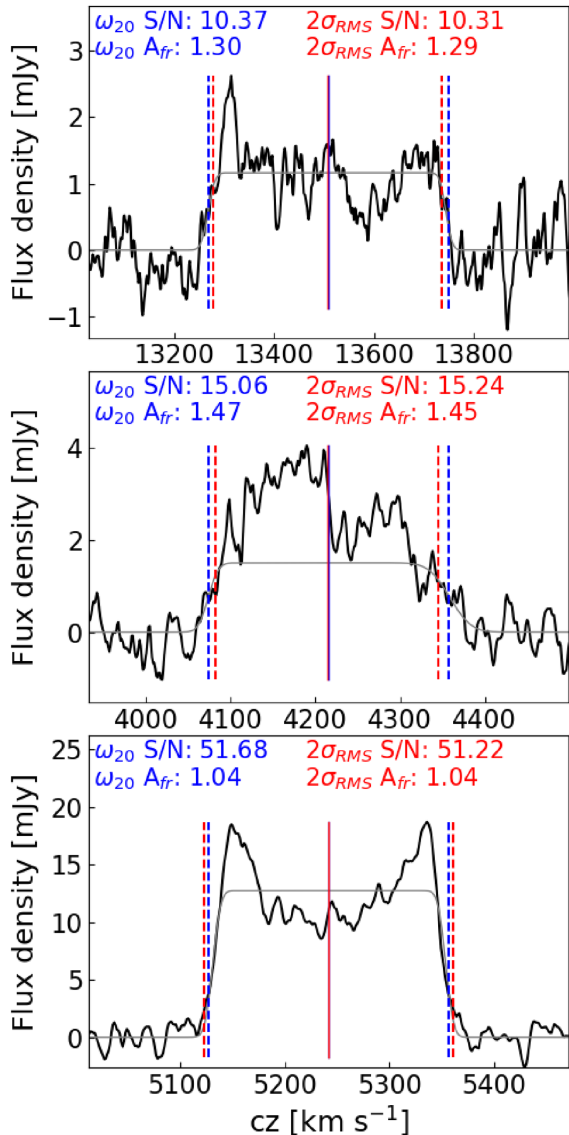
Figure 1. Comparison of measurement limits. Three xGASS spectra with $S/N \sim 10$ (top), $S/N \sim 15$ (middle), and $S/N \sim 51$ (bottom) with measurement limits defined at 20 per cent of the height of the peaks (blue) and at $2\sigma_{\mathrm{RMS}}$ (red). The vertical dashed lines show the locations of V_L and V_U, the thin solid lines the location of V_M, and the coloured text corresponds to the respective S/N and A_{fr} measurements. The thin, grey lines show the busy function fits that are focused on parametrizing only the edges.

function fits can be seen in Fig. 1 as the thin, grey lines. We define lower (V_L) and upper (V_U) velocity limits for the spectra as where the busy function fit equals twice the RMS noise ($2\sigma_{\mathrm{RMS}}$), measured in the signal-free part of the data, and taking the difference of these limits we measure the velocity width (ω) and integrating between them we measure the integrated flux (S_{int}).

We computed the median and median absolute deviation (multiplied by 1.4826 to convert to a standard deviation, σ_{MAD}) of the difference between our S_{int} measurements and the ALFALFA catalogue values, and selected any spectra with more than a 1 σ_{MAD} difference from the ALFALFA S_{int} value as outliers, and all cases where at least one of the error function terms in the busy function

fit was <0.2,[1] as this typically means it has not meaningfully fit the edges of the spectrum. We manually intervened in these fits, and boxcar smoothed the spectra or fixed fit parameters as necessary to parametrize the edges.

Using our measurements, we computed the integrated signal-to-noise ratio of each spectrum (S/N, Saintonge 2007)

$$S/N = \frac{S_{\mathrm{int}}/\omega}{\sigma_{\mathrm{RMS}}} \sqrt{\frac{1}{2} \frac{\omega}{V_{\mathrm{sm}}}}, \qquad (1)$$

where V_{sm} is the final velocity resolution of the spectrum after boxcar smoothing. To measure asymmetry we define the middle velocity $V_M = (V_L + V_U)/2$, and compute the ratio of integrated flux in each half of a spectrum

$$A = \frac{\int_{V_M}^{V_U} S_v \mathrm{d}v}{\int_{V_L}^{V_M} S_v \mathrm{d}v}, \qquad (2)$$

which we use to define the integrated flux ratio asymmetry parameter (e.g. Haynes et al. 1998; Watts et al. 2020a):

$$A_{\mathrm{fr}} = \begin{cases} A & A \geq 1 \\ 1/A & A < 1 \end{cases}. \qquad (3)$$

This definition of A_{fr} removes the left-/right-handedness inherent to the ratio A, such that a perfectly symmetric spectrum has $A_{\mathrm{fr}} = 1$ and values of $A_{\mathrm{fr}} > 1$ indicate deviation from symmetry.

To define our ALFALFA sample, we selected 2742 galaxies with $S/N \geq 10$ to avoid low-quality spectra and reduce uncertainty in the measurement of A_{fr} (Watts et al. 2020a). We removed a further 251 (9 per cent) galaxies that had measurement limits separated by less than 20 channels (i.e. narrower than 110 km s^{-1}) to avoid the regime where A_{fr} cannot be properly determined (Deg et al. 2020), 142 (5 per cent) galaxies that had missing data due to RFI removal that overlapped the H I spectral line, and a further 98 (4 per cent) that did not have well-defined edges and could not be fit, leaving 2251 galaxies in our sample (82 per cent). Last, we assessed our ALFALFA sample for H I confusion by cross-matching each galaxy to all objects with $\log (M_\star/M_\odot) \geq 8.5$ in the MPA/JHU VAC within a tolerance of 2 arcmin and 200 km s^{-1}. A total of 219 galaxies had at least one companion within these limits, and we removed 191 with companions bluer than the $g - r$ colour cut-off Zu & Mandelbaum (2016) used to separate blue- and red-sequence galaxies,

$$g - r < 0.8 \left(\frac{\log M_\star}{10.5} \right)^{0.6}, \qquad (4)$$

using the SDSS model magnitudes of each companion. Only galaxies with blue companions are removed, as their colour indicates that they are star forming and thus host cold gas that could contribute non-negligible H I emission to the spectrum of the target galaxy, while red companions are likely to be passive and not host significant cold gas. We inspected the 2032 galaxies with no identified companions and removed 76 clear cases of confusion where the companion is not part of the SDSS DR7 catalogue. Thus, the final number of galaxies in our ALFALFA sample is 1984.[2]

The post-merger galaxies were fit using the same procedure, and the quality cuts reduced the sample size from 75 galaxies to 45.

---

[1]This is not a universal threshold as some Gaussian-shaped spectra are fit well by this parameter value, but a value identified from visual inspection of cases where straight-edged spectra are incorrectly fit.

[2]We also tested stricter confusion limits of 3 arcmins and 300 km s^{-1}, which removes $\sim$200 more galaxies, and found no quantitative changes to our results.

We utilized the busy function fits to xGASS spectra from Watts et al. ([2020a](#)), remeasured them using $2\sigma_{\mathrm{RMS}}$ measurement limits, and applied the same quality cuts to ensure consistency between the samples, leaving 399 galaxies. Both the post-merger and xGASS catalogues have already been assessed for H I confusion. We refer to these samples of 1984, 399, and 45 galaxies as the parent samples for ALFALFA, xGASS, and the post-mergers, respectively.

Finally, we note that our velocity limits are not a 'standard' choice for H I studies, which typically adopt some fraction of the peak(s) in the spectrum. The values of these peak(s) are not immune to elevation or suppression due to noise, particularly at low *S/N*, and we have not parametrized them with our busy function fits. In Fig. [1](#), we show how our velocity limits compare to the choice of 20 per cent of a spectrum's peak(s), as adopted by Watts et al. ([2020a](#)) for xGASS, for three different *S/N* spectra. Clearly, there is no significant difference between the locations of the limits, or the resulting measurements of *S/N* or A_{fr} in these examples. We also compared the differences in these measurements for our whole xGASS sample and found a median and σ_{MAD} of 0.017 and 0.124 for *S/N*, and -0.0016 and 0.014 for A_{fr}, respectively.

3.2 Star-forming main-sequence selection

To study galaxies that have not undergone significant suppression of their SFR, we restrict our samples to the SFMS. To do so, we use the fits by Janowiecki et al. ([2020](#)) to the xGASS specific SFR (sSFR = SFR/$M_\star$) SFMS

$$\log \mathrm{sSFR}_{\mathrm{MS}}\,[\mathrm{yr}^{-1}] = -0.344(\log(M_\star/\mathrm{M}_\odot) - 9) - 9.822, \quad (5)$$

and its scatter

$$\sigma_{\mathrm{MS}}[\mathrm{yr}^{-1}] = 0.088(\log(M_\star/\mathrm{M}_\odot) - 9) + 0.188, \quad (6)$$

and select galaxies with $\log \mathrm{sSFR}\,[\mathrm{yr}^{-1}] \geq \log \mathrm{sSFR}_{\mathrm{MS}} - 1.5\sigma_{\mathrm{MS}}$ from the SFMS. Namely, galaxies more star forming than $1.5\sigma_{\mathrm{MS}}$ *below* the SFMS. The final number of galaxies in the SFMS sub-samples for ALFALFA, xGASS, and the post-mergers are 1784, 322, and 38, respectively, which from here we denote as $\mathrm{ALFALFA}_{\mathrm{MS}}$, $\mathrm{xGASS}_{\mathrm{MS}}$, and $\mathrm{PM}_{\mathrm{MS}}$.

In Fig. [2](#), we show the stellar mass versus sSFR plane and H I gas fraction scaling relation for our xGASS, ALFALFA, and post-merger parent samples and SFMS sub-samples, alongside density-normalized probability distributions of the parameters for xGASS and ALFALFA. We do not show the parameter distributions for the post-mergers due to their small sample size. The $\log M_\star$ distributions of ALFALFA and xGASS show that they cover the same $\log M_\star$ range, with xGASS having slightly more lower mass galaxies, and that there are no significant differences between the parent samples and SFMS sub-samples. In the top panel, we see that even before the selection of the SFMS, the xGASS, and ALFALFA parent samples are dominated by main-sequence galaxies. This is unsurprising as we can only measure asymmetry in high *S/N* H I detections, which are more likely to be star-forming systems. Both before and after the sSFR cut the $\log \mathrm{sSFR}$ distribution of both samples are well matched. Post-mergers galaxies are, as expected, preferentially star-forming systems above the SFMS due to the star formation triggered during the merging process (Ellison et al. [2013](#)).

In the bottom panel, the main difference between xGASS and ALFALFA is clear: ALFALFA almost exclusively detects galaxies above the xGASS median[3] H I mass fraction scaling relation, shown
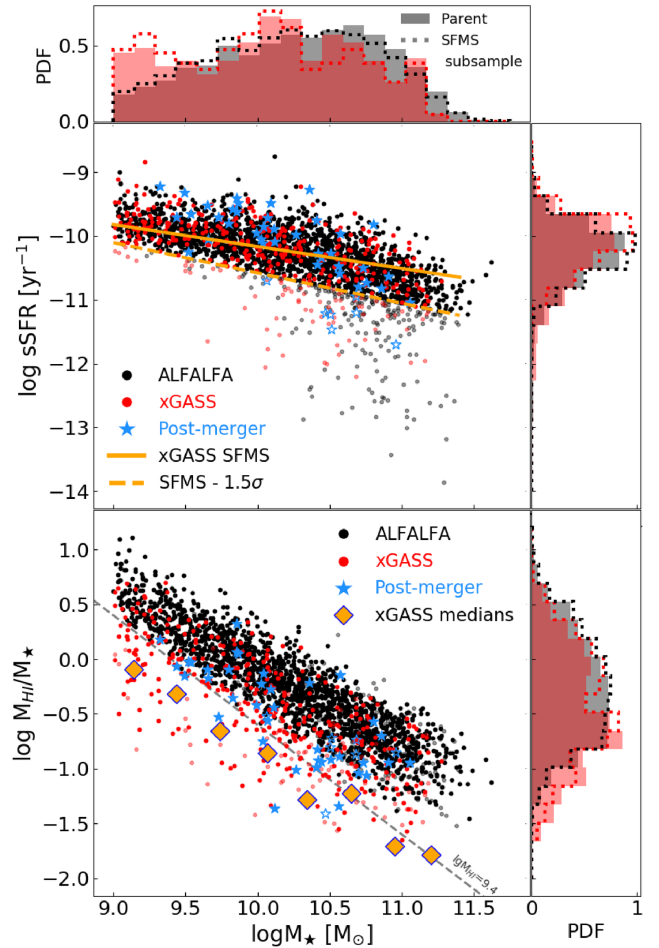
[3]Weighted medians computed including upper limits.

Figure 2. Scaling relations and property distributions of our samples. The top panel shows sSFR as a function of stellar mass, with the xGASS SFMS shown as a solid, orange line. The bottom panel shows the H I mass fraction scaling relation with the xGASS weighted medians (from Catinella et al. [2018](#), computed including non-detections set to their upper limits) shown as the orange diamonds. The density-normalized probability distributions of each parameter are given on the opposite side to their respective axis labels. In both panels, ALFALFA and xGASS are shown as black and red, respectively, and the distinction between the solid/light points or the dotted/filled histograms is by membership to the sub-/parent- samples, where the sub-samples are separated by SFMS-1.5σ as shown by the dashed orange line in the top panel. Post-merger galaxies are shown using filled/open, light blue stars that represent the same sub-/parent- sample membership. The dashed, grey line in the bottom panel corresponds to a constant $\log(M_{\mathrm{H\,I}}/\mathrm{M}_\odot) = 9.4$.

as the orange diamonds. The xGASS parent- and SFMS sub-samples show a similar bias towards galaxies above the median scaling relation, due to being detection selected, but the targeted survey design of xGASS means that there are also galaxies below the medians. Selecting the SFMS causes a slight shift towards higher H I fractions, as gas content and star formation are correlated, but the effect is small for both samples. The $\mathrm{PM}_{\mathrm{MS}}$ sample occupies the same region of the parameter space as xGASS as they have the same survey design and are also detection selected. These $\log(M_{\mathrm{H\,I}}/M_\star)$ distributions demonstrate the advantage of analysing these three samples together: ALFALFA samples the gas-rich regime with high statistics, xGASS extends $0.5-1$ dex lower in H I mass fraction than ALFALFA, and the post-mergers provide strongly

interacting, star-forming galaxies with similar coverage as xGASS. However, it also highlights how a SFMS-selected sample does *not* translate to a clear selection in galaxy H I mass fraction. ALFALFA is not representative of the H I fractions of galaxies within the SFMS, missing the 'gas-poor' tail of star-forming galaxies that is revealed by xGASS, and this will limit our ability to use ALFALFA to look for trends between H I asymmetry and gas content.

3.3 Asymmetric and symmetric galaxies

The uncertainty in an A_{fr} measurement is closely linked to the *S/N* of a spectrum (Watts et al. 2020a), and this must be taken into account when selecting and comparing different samples, particularly if they have different *S/N* distributions. We briefly describe how we model and account for this effect here, but refer the reader to Watts et al. (2020a) for a more detailed description. We also acknowledge that there are other sources of uncertainty on A_{fr} measurements, as mentioned in Watts et al. (2020a), but these are minimized by our *S/N* cut and removal of confused systems, and we do not expect them to impact our results.

A toy model is used to create noiseless, model H I spectra with intrinsic asymmetries ($A_{fr, i}$) of $A_{fr, i} = 1, 1.1$, and 1.25, corresponding to symmetric spectra, asymmetric spectra (Haynes et al. 1998; Watts et al. 2020a), and a higher value to model strongly asymmetric spectra. Mock observations are created by degrading the model spectra to a desired *S/N* by adding Gaussian random noise, and 10^4 noise realizations are created for *S/N* values in the range *S/N* = [5, 100] in steps of $\Delta S/N = 1$, to properly model marginal detections below our *S/N* cut to high *S/N* spectra. The 'observed' *S/N* and A_{fr} of each mock spectrum is calculated using measurement limits defined on the noiseless model spectrum by treating it as a 'fit' to the mock spectra, as the straight edges of H I spectra are typically well defined and not significantly impacted by noise.

In Fig. 3, we show the distribution of recovered A_{fr} measurements as a function of *S/N* for our three modelled $A_{fr, i}$ values. The background density plots show the normalized probability distribution function of recovered A_{fr} measurements in bins of $\Delta \log (S/N) = 0.008$, sampled in bins of $\Delta A_{fr} = 0.0034$, and truncated at their 25th and 75th percentiles (the 50th for the $A_{fr, i} = 1$ model, as it is reflected about $A_{fr} = 1$). The intrinsic asymmetry of each model and the median recovered A_{fr} in bins of $\Delta S/N = 4$ are shown with black ($A_{fr, i} = 1$), red ($A_{fr, i} = 1.1$), and blue ($A_{fr, i} = 1.25$), the solid and dashed lines, respectively. Clearly, the uncertainty in an A_{fr} measurement increases as a *S/N* decreases, and at low *S/N* galaxies preferentially scatter towards *higher* A_{fr} values due to the distributions being bounded by $A_{fr} = 1$. This is visible in the distribution of recovered A_{fr} measurements for the $A_{fr, i} = 1$ model, as the median recovered A_{fr} is >1 for all A_{fr}; and in the $A_{fr, i} = 1.1$ model by the deviation of its median to $A_{fr} > 1.1$, and the upward compression of the low-A_{fr} side of its distribution.

We quantify this scatter in A_{fr} measurements due to noise at a given *S/N* by computing the percentiles of the A_{fr} distribution for all mock spectra in bins of $\Delta S/N = 4$. These percentiles are well described by an inverse power law of the form

$$PXX(S/N, A_{fr,i}) = \frac{1}{a(S/N - b)} + A_{fr,i}, \quad (7)$$

where the constants a and b depend on the desired percentile 'PXX'. We fit these percentiles to parametrize A_{fr} as a function of *S/N* for a given $A_{fr, i}$. It is important to mention that these percentiles are almost completely insensitive to the degree of smoothing and shape of a H I
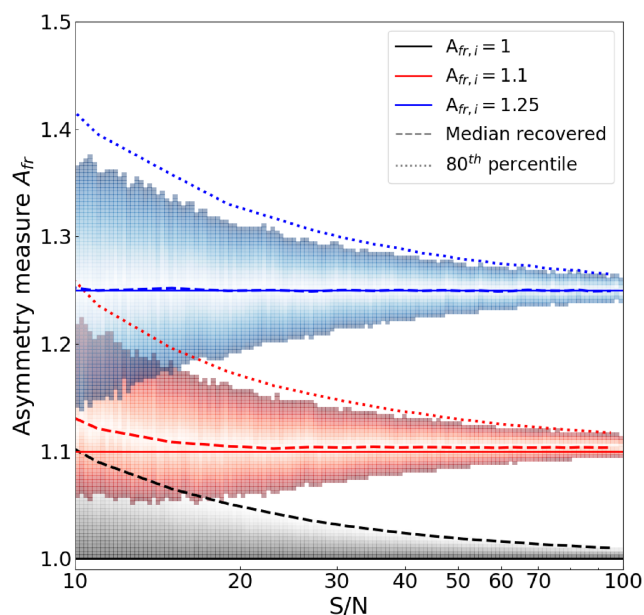

Figure 3. The distribution of recovered A_{fr} measurements as a function of *S/N*. The background density plots show the normalized probability distribution of A_{fr} measurements in bins of $\Delta \log (S/N) = 0.008$ for our model spectra with $A_{fr, i} = 1$ (black), $A_{fr, i} = 1.1$ (red), and $A_{fr, i} = 1.25$ (blue). The density maps are truncated at their 25th and 75th percentiles for $A_{fr, i} = 1.1$ and $A_{fr, i} = 1.25$, and the 50th for $A_{fr, i} = 1$ as it is symmetric about $A_{fr} = 1$. The value of $A_{fr, i}$ for each model is shown with a solid line, and the median recovered value in bins of $\Delta S/N = 4$ are shown as the dashed lines. The 80th percentiles of the $A_{fr, i} = 1.1$ and 1.25 models, used to select our asymmetric and strong-asymmetry populations, respectively, are shown with the dotted lines.

spectrum, so long as they are parametrized as a function of *S/N* as defined in equation 1 (Watts et al. 2020a).

Utilizing this model, we select asymmetric and symmetric populations from each SFMS sub-sample using the same thresholds as Watts et al. (2020a), with an additional 'strong-asymmetry' population to investigate the properties of the most asymmetric galaxies:

(i) The symmetric population is selected as $A_{fr} \leq P50(S/N, A_{fr, i} = 1$; i.e. the median), as 50 per cent of intrinsically symmetric spectra will have A_{fr} below this percentile.

(ii) The asymmetric population is defined as $A_{fr} \geq P80(S/N, A_{fr, i} = 1.1)$, i.e. galaxies that have at least 10 per cent intrinsic asymmetry to at least an 80 per cent confidence level, considering noise.

(iii) The strong-asymmetry population is defined as $A_{fr} \geq P80(S/N, A_{fr, i} = 1.25)$, namely at least 25 per cent intrinsic asymmetry with 80 per cent confidence.

These selections are visible in Fig. 3 as the black-dashed (symmetric), dotted red (asymmetric), and dotted blue (strong-asymmetry) lines. There will be some contamination of the symmetric population, particularly at lower *S/N*, but we must compromise between sample size and purity, and the deviation from symmetry shown by these galaxies is small compared to the effect of noise, so we do not expect them to affect our results. Fig. 3 also demonstrates why it is necessary to use these percentiles to select our populations, as they increase the confidence in the separation of intrinsically symmetric and asymmetric galaxies. At *S/N* = 10, a galaxy with A_{fr} = 1.1 has a 50 per cent chance of having $A_{fr, i} = 1$, namely being intrinsically symmetric. Similarly, a galaxy with A_{fr} = 1.25 has a 20 per cent chance of having $A_{fr} = 1.1$, namely it is asymmetric,

but not strongly asymmetric, as might be inferred if the effect of noise was not accounted for. Thus, the number of galaxies in the asymmetric and symmetric populations, respectively, are 121 and 87 for xGASS$_{\rm MS}$, 12 and 8 for PM$_{\rm MS}$, and 541 and 431 for ALFALFA$_{\rm MS}$. The strong-asymmetry population is only defined for ALFALFA$_{\rm MS}$, and consists of 168 galaxies.

3.4 Offset parameters

We quantify the difference in the H I and star formation properties of asymmetric galaxies compared to symmetric ones with a matched-galaxy offset analysis (e.g. Ellison et al. 2018; Watts et al. 2020a), using only galaxies within the SFMS. Each asymmetric galaxy is matched to all symmetric galaxies within 0.1 dex in log ($M_\star/{\rm M}_\odot$) and log S/N, and if less than five symmetric galaxies are matched then we expand these tolerances by 0.1 and 0.05 dex, respectively, until at least five matches are found. Typically, > 80 per cent of galaxies find sufficient matches without needing to increase the tolerances in ALFALFA$_{\rm MS}$, and with only one expansion in xGASS$_{\rm MS}$ due to the smaller sample size. The S/N match is included because lower S/N galaxies typically have higher $A_{\rm fr}$ due to the effect of noise and, in xGASS, there is a correlation where higher S/N galaxies typically have higher H I content. This correlation is also present in xGASS$_{\rm MS}$, and if left uncorrected it could bias us towards inferring higher $A_{\rm fr}$ galaxies are more gas-poor. This correlation is not present in ALFALFA$_{\rm MS}$ and we note that removing the S/N matching does not change our results, but we keep it for consistency between analyses and with previous work. Last, we allow galaxies with $S/N \geq 40$ to match to other galaxies with $S/N \geq 40$ regardless of S/N, as the effect of noise on $A_{\rm fr}$ is small above this value, and to avoid discarding the fewer high S/N spectra.

The H I mass fraction ($\Delta f_{\rm gas}$) and sSFR (ΔsSFR) offsets are then defined as the logarithmic difference between the value for the asymmetric galaxy, and the median of the matched symmetric galaxies:

$$\Delta f_{\rm gas} = \log(M_{\rm H\,I}/M_\star)_{\rm asym} - {\rm med}[\log(M_{\rm H\,I}/M_\star)_{\rm sym,match}] \qquad (8)$$

$$\Delta{\rm sSFR} = (\log {\rm sSFR})_{\rm asym} - {\rm med}[(\log {\rm sSFR})_{\rm sym,match}]. \qquad (9)$$

In this way, we compare the properties of asymmetric galaxies to what would be expected for a symmetric galaxy at fixed $M_\star$ and S/N. We also compute these offsets for each symmetric galaxy using the same process, to inform us about the distribution of the symmetric population.

4 RESULTS

4.1 Global H I asymmetries on the SFMS

We first focus on the properties of galaxies in the ALFALFA$_{\rm MS}$ sample. In Fig. 4, we show the $\Delta f_{\rm gas}-\Delta$sSFR parameter space for the ALFALFA$_{\rm MS}$ sample, where the asymmetric and strongly asymmetric samples are matched to the symmetric sample, and the symmetric sample matched to itself. We show thin, black lines at $\Delta f_{\rm gas} = \Delta$sSFR $= 0$ to provide a visual centre of the parameter space, and the dotted, black lines at ± 0.5 to demonstrate the extent of the scatter. To the top and right of the central panel, we show density-normalized probability distributions of each offset parameter and extensions of the $\Delta f_{\rm gas} = \Delta$sSFR $= 0$ and ± 0.5 lines. Surrounding the main panel, we show SDSS cut-outs and global H I spectra of example (strongly) asymmetric and symmetric galaxies, to show the diversity of optical properties of galaxies in the parameter space.

These example galaxies are paired according to their similar $\Delta f_{\rm gas}$ and ΔsSFR, denoted by the large, bordered, markers that are shown both in the main panel and inset beside their spectrum, with a thin, black line connecting each pair to its location in the parameter space.

Clearly, the bulk of the symmetric and asymmetric populations are contained within $\Delta f_{\rm gas} = \Delta$sSFR $= \pm 0.5$. The only clear deviation outside this scatter is for ΔsSFR > 0.5, and this part of the parameter space is occupied by both asymmetric and symmetric galaxies. This is also reflected in the distributions of each offset parameter. The $\Delta f_{\rm gas}$ distributions are centred on zero with similar widths, while the asymmetric galaxies show slightly higher ΔsSFR values. To provide quantitative comparisons, we calculate the median offsets of the asymmetric population with uncertainty derived from 10^4 bootstraps and perform a two-sample Kolmogorov–Smirnov test (KS-test) between the asymmetric and symmetric populations. These medians, and the KS-test D-statistics and p-values are listed in Table 1. The median offsets for the asymmetric population are small, $\Delta f_{\rm gas} = 0.01 \pm 0.01$ with $p = 0.45$ and ΔsSFR $= 0.04 \pm 0.02$ with $p = 0.03$, though the KS-test result indicates that the ΔsSFR distribution of asymmetric galaxies is different to that of symmetric ones.

It is important to note that the lack of galaxies with ΔsSFR < -0.5 and $\Delta f_{\rm gas} < -0.5$, shown as the grey-shaded regions in the main panel of Fig. 4, is simply due to the fact that ALFALFA does not reach lower (relative) gas fractions and our sample is only representative of the SFMS. However, despite restricting our sample to the most gas-rich and star-forming systems, we can already conclude that global H I asymmetries are not preferentially found in gas-rich or highly star-forming objects.

In Fig. 4, we also highlight the subset of asymmetric galaxies with strong asymmetry, to investigate the properties of the most disturbed systems. This population spans the same $\Delta f_{\rm gas}$ and ΔsSFR ranges as the asymmetric and symmetric populations, and the offset distributions show little difference from the asymmetric population aside from a small increase in positive offset values. The median offsets for this population are $\Delta f_{\rm gas} = 0.05 \pm 0.02$ with $p = 0.11$ and ΔsSFR $= 0.12 \pm 0.03$ with $p = 9 \times 10^{-4}$, indicating that a significant offset is only present in sSFR, not H I fraction. This suggests that greater $A_{\rm fr}$ is associated with greater ΔsSFR. To further confirm this, we performed the same analysis on the subset of the asymmetric population after *removing* the strong asymmetry galaxies. We find that this remaining subset of 373 galaxies has a median ΔsSFR $= 0.02 \pm 0.02$, namely consistent with no elevation in ΔsSFR, and the KS-test $p = 0.45$ cannot determine that the ΔsSFR distribution is different to that of symmetric galaxies. Thus, the difference in ΔsSFR between symmetric and asymmetric galaxies is primarily driven by galaxies with the highest $A_{\rm fr}$.

The example galaxies surrounding Fig. 4 highlight the diversity in the optical properties of symmetric and strongly asymmetric galaxies across the parameter space. Both populations show signatures of optical disturbances, blue star-forming discs, and apparent prominence of the bulge. There is no clear distinction in the optical morphologies of galaxies whether they are classified as symmetric or asymmetric, and this diversity is present across the parameter space. Thus, we emphasize here the main result of this work. Any physical process(es) driving H I disturbances in the gas-rich regime on the SFMS are only evident in the highest $A_{\rm fr}$ systems, and only appear to impact the star formation properties of galaxies with no measurable impact on their H I content.

The complexity of the link (or lack thereof) between H I asymmetry and other galaxy properties is further highlighted by our sample of post-merger galaxies. Our small sample size does not permit any
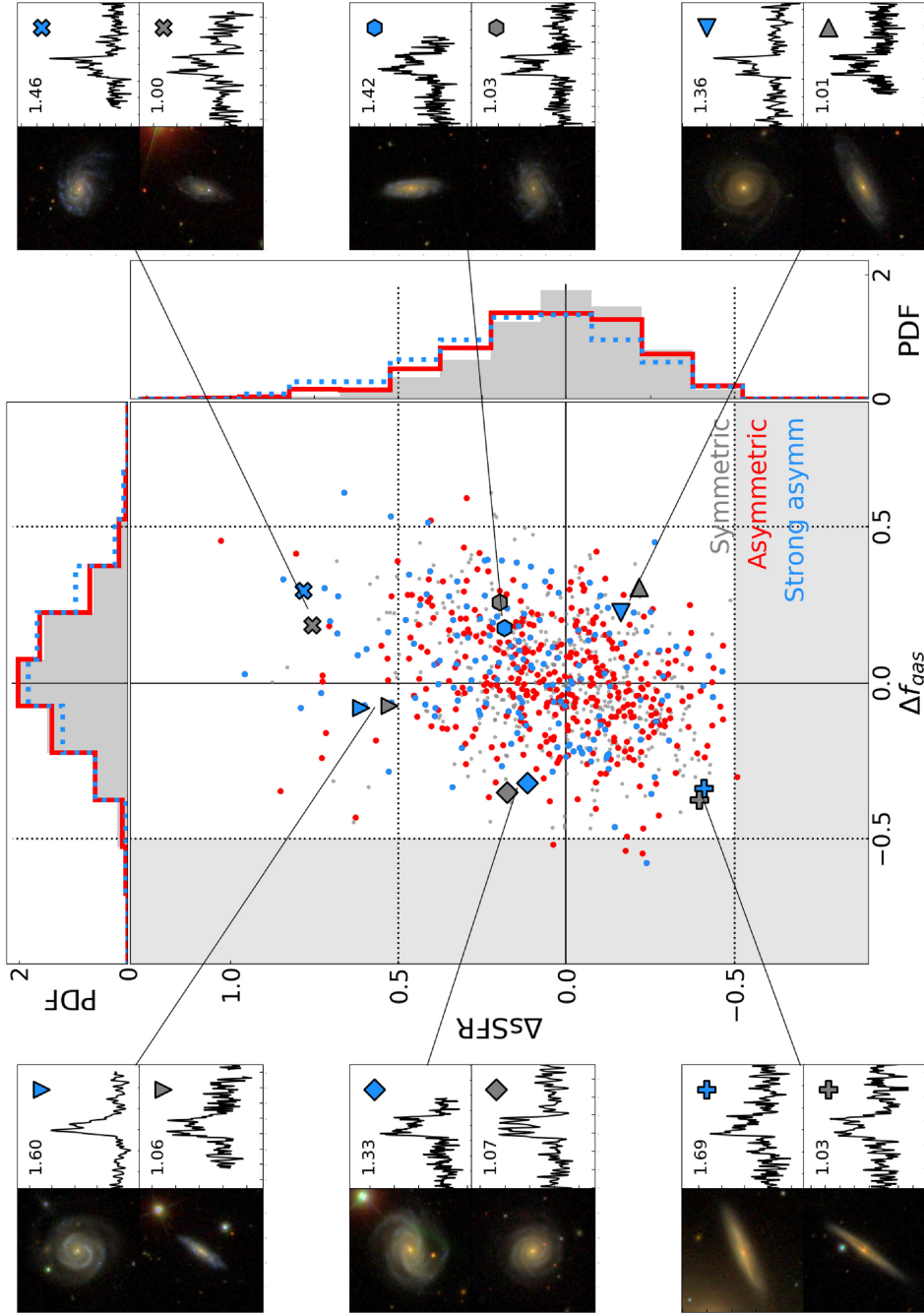
Figure 4. $\Delta f_{gas} - \Delta sSFR$ parameter space for ALFALFA$_{MS}$ galaxies. The central panel shows the location of galaxies in the parameter space, and the density-normalized probability distribution of each offset parameter is shown opposite to their respective axis label. Symmetric galaxies are shown with the grey points and the filled histograms, asymmetric galaxies with the red points and the red, open histograms, and the subset of the asymmetric population with strong asymmetry as the light blue points and the dotted, open histograms. The horizontal and vertical black, dotted lines correspond to ±0.5 for each offset parameter, and the grey, shaded regions denote offsets of <-0.5 that are sparsely populated due to our sample selection criteria. SDSS cut-outs (1.5 arcmin^2) and global H I spectra, for example, asymmetric and symmetric galaxies are shown to either side of the main panel, and the A_{fr} value of each spectrum is given to their top left. The example galaxies are paired by their similar offset values, as indicated by the thin, black line connecting each pair to their location in the parameter space, and the large, bold markers in the parameter space that match the symbol next to their spectrum.

Table 1. Median offset parameters and two-sample Kolomogorov-Smirnov test D- and p-values for the populations presented in Sections 4.1 and 4.2.

Sample	Offset	Median	D-value	p-value
AA$_{MS}$ asymmetric	Δf_{gas}	0.01 ± 0.01	0.05	0.45
	ΔsSFR	0.04 ± 0.02	0.09	0.03
AA$_{MS}$ strong asymm	Δf_{gas}	0.05 ± 0.02	0.11	0.11
	ΔsSFR	0.12 ± 0.03	0.18	9×10^{-4}
xGASS$_{MS}$ asymmetric	Δf_{gas}	-0.13 ± 0.03	0.22	0.03
	ΔsSFR	0.03 ± 0.04	0.15	0.22

statistical comparisons, so in Fig. 5 we show the five highest A_{fr} and the five most H I symmetric PM$_{MS}$ galaxies. The fact that PM$_{MS}$ galaxies span the same range of asymmetries – from almost perfectly symmetric to highly asymmetric – demonstrates that the presence of optical disturbance in a galaxy does not necessarily imply elevated H I asymmetry, and vice versa. While merger activity can enhance global H I asymmetry on a statistical level (e.g. Bok et al. 2019), projection effects (e.g. Deg et al. 2020) or the settling of the gas back into regular rotation in advanced merging stages (e.g. Manthey et al. 2008; Schiminovich, van Gorkom & van der Hulst 2013) could be responsible for symmetric H I spectra, even when signatures of the merger remain in optical images, or stellar or ionized gas kinematics (e.g. Feng et al. 2020; Nevin et al. 2021).

4.2 Comparison with xGASS

The results presented in the previous section may appear in contradiction with the recent work by Watts et al. (2020a) who, using xGASS, found that H I asymmetries are preferentially found in gas-poor galaxies. Here, we discuss how these two results can be easily reconciled. In Fig. 6, we show the $\Delta f_{gas}-\Delta$sSFR parameter space for xGASS$_{MS}$. As in ALFALFA$_{MS}$, there are some galaxies with ΔsSFR > 0.5, though the median offset ΔsSFR $= 0.03 \pm 0.04$ with $p = 0.22$ is small, and we cannot determine that the two distributions are different. The most significant difference compared to ALFALFA$_{MS}$ is that the asymmetric population preferentially inhabits the $\Delta f_{gas} < 0$ half of the parameter space, and there are now clearly galaxies with $\Delta f_{gas} < -0.5$. This is evident in the Δf_{gas} distribution, which has a median $\Delta f_{gas} = -0.13 \pm 0.03$ and $p = 0.03$ suggesting that the asymmetric galaxies have a different distribution from the symmetric ones. This reflects the sensitive H I observations of xGASS and the fact that a SFMS-selected sample does not translate to a clear selection in H I mass fraction. We demonstrate this by highlighting galaxies below an ALFALFA-like H I mass limit of $\log(M_{HI}/M_\odot) = 9.4$ (shown in the H I mass fraction scaling relation panel of Fig. 2 with a grey, dashed line) with the orange points in Fig. 6. These galaxies constitute all but one of the $\Delta f_{gas} < -0.5$ points, and all apart from two have $\Delta f_{gas} < 0$, showing that the 'gas-poor' tail of the SFMS drives the suppressed H I content of asymmetric galaxies. Thus, in terms of their gas content, asymmetric galaxies preferentially scatter towards lower H I fractions, but evidencing this requires deep H I observations that are not typically reached by blind H I surveys. The xGASS$_{MS}$ sample is consistent with ALFALFA$_{MS}$ once selection biases are properly taken into account.

5 DISCUSSION AND CONCLUSIONS

In this work, we have investigated the shape of global H I spectra, through measurement of their asymmetry, in a data set that samples

the gas-rich regime with high statistics, covers ~ 2 dex in H I mass fraction, and provides insight into strong gravitational interactions. In particular, we have determined whether elevated global H I asymmetry in galaxies is also associated with a change in their H I content or sSFR. Our key result is that at fixed stellar mass, in the gas-rich regime, and on the SFMS, there is no systematic difference in the H I content of galaxies with asymmetric global H I spectra compared to symmetric ones. It is only mechanisms that disturb and remove the H I that cause a clear, systematic, difference in the H I content of H I asymmetric galaxies, and this requires observations that measure H I fractions below the median scaling relations of representative samples. There is some evidence for elevated sSFR in H I asymmetric galaxies, and this is primarily driven by galaxies with the highest H I asymmetry. There is also no clear correlation between optical morphology and global H I asymmetry, and post-merger galaxies, despite being strongly disturbed systems optically, show a range of H I asymmetries.

Gas accretion has been proposed as a mechanism that could drive the ubiquity of disturbances in the H I in galaxies. Matthews et al. (1998) found that 77 per cent of late-type galaxies had asymmetric global H I spectra, while Haynes et al. (1998) found 45 per cent in isolated galaxies in general. As late-type galaxies are typically more H I rich, this has been interpreted as the signature of accretion-driven asymmetries. We find no evidence for an elevation in the H I content of galaxies with asymmetric H I spectra in the gas-rich regime, in agreement with Reynolds et al. (2020b). The difference in these results could be explained by the smaller sample sizes and the lack of compensation for measurement noise that *must* be taken into account when comparing asymmetry rates. A total of 57 per cent of our ALFALFA spectra have $A_{fr} \geq 1.1$, but after accounting for noise with the asymmetric population (before SFMS selection), i.e. 80 per cent confidence that their $A_{fr} \geq 1.1$, this is reduced to 29 per cent. To the same threshold, xGASS and xGASS isolated galaxies show asymmetry rates of 37 per cent and 32 per cent, respectively. Thus, gas-rich galaxies do not show a higher rate of H I asymmetry than a sample that is more representative of the H I fractions of galaxies, even when restricted to isolated systems. Assuming that gas-richness is a consequence of gas accretion, this implies that either gas accretion is not a dominant driver of global H I asymmetry or that, if it is, it affects more the dynamics of the H I reservoir (causing asymmetry in global spectra) than its H I content. Simulations of gas accretion on the galaxy scale have shown that, by mass, the dominant channel of gas accretion on to galaxies is through the accretion of satellite galaxies (Nelson et al. 2013, 2015). This scenario brings additional gravitational perturbation to the picture, and the repeated merging of these satellites has been proposed to explain the ubiquity of disturbances in galaxies (Zaritsky & Rix 1997). Bassett et al. (2017) showed that gas accreted on to a gas-rich galaxy will settle into co-rotating orbits, causing a smaller perturbation, whereas accretion on to a gas-poor galaxy allows the gas to retain memory of its accretion history, potentially causing greater asymmetry. Whether it is the active accretion of satellites, particularly those below the detection limit of many optical surveys (e.g. Portas et al. 2011; Ramírez-Moreta et al. 2018), the ongoing response to perturbations in the gravitational potential of the dark matter halo caused by these accretions (e.g. van Eymeren et al. 2011), or a combination of both (Zaritsky et al. 2013), remain unknown. Unfortunately, the marginal increase in sSFR that we have observed in galaxies with the strongest asymmetry cannot discriminate between these two scenarios, as both can cause increased sSFR (e.g. Jog 1997; Cox et al. 2008).

Current cosmological-hydrodynamical simulations of galaxy formation are well suited to investigating H I asymmetry in the
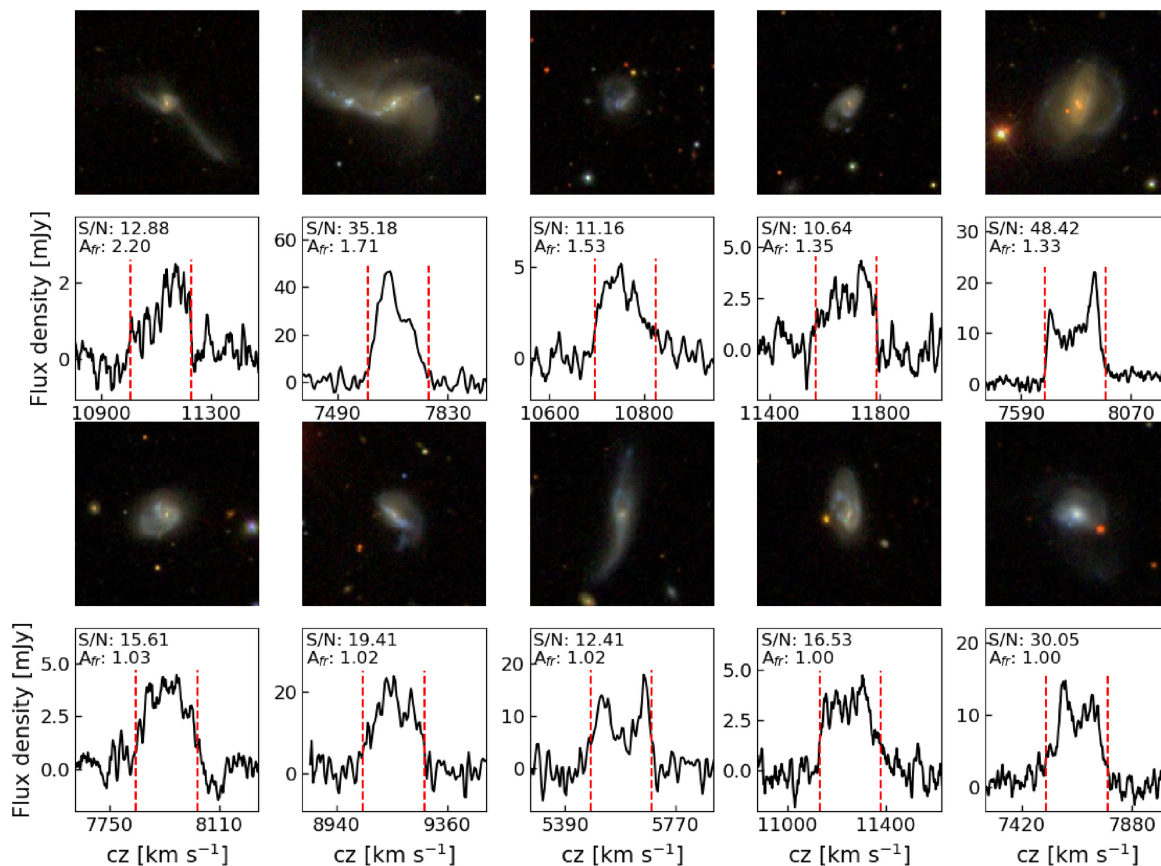
Figure 5. SDSS cut-outs (1.5 arcmin^2) and global H_I spectra of the five highest A_{fr} (top row) and five most symmetric (bottom row) PM$_{MS}$ galaxies. The *S/N* and A_{fr} values are given in the top left of each spectrum.
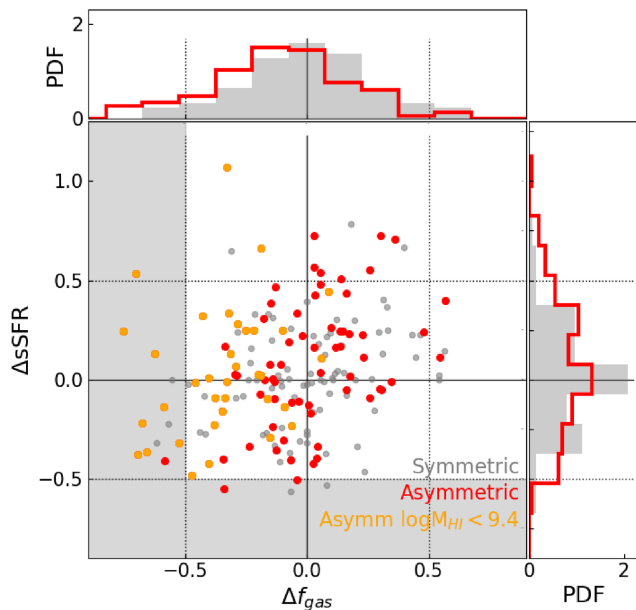
gas-rich regime (e.g. Watts et al. 2020b), and the relationship between gas accretion, tidal interactions, and global H_I asymmetry in these cosmological volumes remain to be quantified. Furthermore, determining how disturbances move across the stellar, ionized, atomic, and molecular gas components of galaxies is an exciting prospect for future multiwavelength observations.

ACKNOWLEDGEMENTS

DATA AVAILABILITY

The data that support the findings of this study are available upon request from the corresponding author, ABW.

Figure 6. The $\Delta f_{gas} - \Delta$sSFR parameter space as in Fig. 4, but for xGASS$_{MS}$. Asymmetric galaxies with H_I masses below $\log(M_{H_I}/M_{\odot}) = 9.4$, defined using the grey, dashed line in Fig. 2 are highlighted with the orange points.

REFERENCES

Abazajian K. N. et al., 2009, ApJS, 182, 543
Barnes D. G. et al., 2001, MNRAS, 322, 486
Bassett R., Bekki K., Cortese L., Couch W., 2017, MNRAS, 471, 1892

Bok J., Blyth S.-L., Gilbank D. G., Elson E. C., 2019, MNRAS, 484, 582
Catinella B. et al., 2018, MNRAS, 476, 875
Chung A., van Gorkom J. H., Kenney J. D. P., Vollmer B., 2007, ApJL, 659, L115
Cortese L., Catinella B., Cook R. H. W., Janowiecki S., 2020, MNRAS, 494, L42
Cox T. J., Jonsson P., Somerville R. S., Primack J. R., Dekel A., 2008, MNRAS, 384, 386
Darg D. W. et al., 2010, MNRAS, 401, 1552
de Blok W. J. G. et al., 2020, A&A, 643, A147
Deg N., Blyth S. L., Hank N., Kruger S., Carignan C., 2020, MNRAS, 495, 1984
Ellison S. L., Mendel J. T., Patton D. R., Scudder J. M., 2013, MNRAS, 435, 3627
Ellison S. L., Catinella B., Cortese L., 2018, MNRAS, 478, 3447
Espada D., Verdes-Montenegro L., Huchtmeier W. K., Sulentic J., Verley S., Leon S., Sabater J., 2011, A&A, 532, A117
Feng S., Shen S.-Y., Yuan F.-T., Riffel R. A., Pan K., 2020, ApJL, 892, L20
Giovanelli R. et al., 2005, AJ, 130, 2598
Haynes M. P., Hogg D. E., Maddalena R. J., Roberts M. S., van Zee L., 1998, AJ, 115, 62
Haynes M. P. et al., 2018, ApJ, 861, 49
Janowiecki S., Catinella B., Cortese L., Saintonge A., Brown T., Wang J., 2017, MNRAS, 466, 4795
Janowiecki S., Catinella B., Cortese L., Saintonge A., Wang J., 2020, MNRAS, 493, 1982
Jog C. J., 1997, ApJ, 488, 642
Jog C. J., Combes F., 2009, Phys.Rep., 471, 75
Koribalski B. S. et al., 2020, ApSS, 365, 118
Manthey E., Aalto S., Hüttemeister S., Oosterloo T. A., 2008, A&A, 484, 693
Martin D. C. et al., 2005, ApJ, 619, L1
Matthews L. D., van Driel W., Gallagher J. S. I., 1998, AJ, 116, 1169
Meyer M. J. et al., 2004, MNRAS, 350, 1195
Nair P. B., Abraham R. G., 2010, ApJS, 186, 427
Nelson D., Vogelsberger M., Genel S., Sijacki D., Kereš D., Springel V., Hernquist L., 2013, MNRAS, 429, 3353
Nelson D., Genel S., Vogelsberger M., Springel V., Sijacki D., Torrey P., Hernquist L., 2015, MNRAS, 448, 59

Nevin R. et al., 2021, preprint (arXiv:2102.02208)
Portas A. et al., 2011, ApJ, 739, L27
Ramírez-Moreta P. et al., 2018, A&A, 619, A163
Reynolds T. N., Westmeier T., Staveley-Smith L., Chauhan G., Lagos C. D. P., 2020a, MNRAS, 493, 5089
Reynolds T. N., Westmeier T., Staveley-Smith L., 2020b, MNRAS, 499, 3233
Richter O. G., Sancisi R., 1994, A&A, 290, L9
Saintonge A., 2007, AJ, 133, 2087
Salim S. et al., 2016, ApJS, 227, 2
Salim S., Boquien M., Lee J. C., 2018, ApJS, 859, 11
Sancisi R., Fraternali F., Oosterloo T., van der Hulst T., 2008, A&AR, 15, 189
Schiminovich D., van Gorkom J. H., van der Hulst J. M., 2013, AJ, 145, 34
Simard L., Mendel J. T., Patton D. R., Ellison S. L., McConnachie A. W., 2011, ApJS, 196, 11
Swaters R. A., Schoenmakers R. H. M., Sancisi R., van Albada T. S., 1999, MNRAS, 304, 330
van Eymeren J., Jütte E., Jog C. J., Stein Y., Dettmar R. J., 2011, A&A, 530, A30
Walter F., Brinks E., de Blok W. J. G., Bigiel F., Kennicutt, Robert C. J., Thornley M. D., Leroy A., 2008, AJ, 136, 2563
Wang J. et al., 2014, MNRAS, 441, 2159
Watts A. B., Catinella B., Cortese L., Power C., 2020a, MNRAS, 492, 3672
Watts A. B., Power C., Catinella B., Cortese L., Stevens A. R. H., 2020b, MNRAS, 499, 5205
Westmeier T., Jurek R., Obreschkow D., Koribalski B. S., Staveley-Smith L., 2014, MNRAS, 438, 1176
Wong O. I. et al., 2006, MNRAS, 371, 1855
Wright E. L. et al., 2010, AJ, 140, 1868
York D. G. et al., 2000, AJ, 120, 1579
Zaritsky D., Rix H.-W., 1997, ApJ, 477, 118
Zaritsky D. et al., 2013, ApJ, 772, 135
Zu Y., Mandelbaum R., 2016, MNRAS, 457, 4360

This paper has been typeset from a TEX/LATEX file prepared by the author.